Towards a distributed magnetic tactile sensor network for flexible skin

Nuno Lopes
nuno.s.lopes@tecnico.ulisboa.pt

Instituto Superior Técnico, Lisboa, Portugal

November 2021

Abstract

Tactile sensors are of increasingly vital importance in fields such as robotics, to answer the needs of robotic systems in adapting to unstructured environments. In this work, following a biomimetic approach based on human skin, a tactile sensor is developed consisting in a matrix of 4×4 tunnel magnetoresistive sensors which detect the change in magnetic field in a magnetized elastomer, with the magnetic moment set to the sensors' sensitive direction, when it is actuated by a force. It is also studied the influence of 4 different elastomer magnetization configurations. The sensors' ability to detect force intensity and location is demonstrated by using supervised learning algorithms. The intensity of normal forces is estimated with a minimum mean absolute error of approximately 0.023N and a maximum of 0.1N, for forces ranging from 0N to approximately 4N among different magnetization configurations. The ability of differentiating the location of 5 different application points of the force was also observed with a minimum accuracy of 97% among the magnetization configurations. A simulation model was also devised which was able to determine the response of magnetized elastomer to an applied force. Finally, the results of this model were validated against experimental data obtain. **Keywords:** Tunnel Magnetoresistive sensor, flexible skin, distributed magnetization, tactile sensor

1. Introduction

As the field of robotics evolves, tactile sensing's role in this area also gains increased importance. The environment with which robots interact is often times unstructured and the demand is high for technologies that, by helping robots gain an increased perception of their surroundings, can help make these interactions safer whether they are with objects or humans [2].

To help materialize this objective, a biomimetic approach is often followed by researchers which results in the development of different technologies such as cilia or artificial skins that can mimic structures with the same purpose already found in nature and, in particular, humans.

Moreover, the research and development of magnetoresistive sensors has seen tremendous advances in the last decades. In particular tunnel magnetoresistance sensors could be used to increase the sensitivity of tactile sensors.

Although there is not a definition of characteristics these tactile technologies should possess, they should be able to detect forces, with high sensitivity and wide range and in a wide contact area. They should also be simple to avoid complex electronics and bulky data processing centers. As such, in this work a force sensor is developed, composed of a flexible magnetized skin structure placed on top of a 4x4 array of 1-dimensional sensing TMR sensor (as shown in Figure 1). It detects the changing direction of the free layer's magnetization due to variations in the external magnetic field caused by deformations in the artificial skin when forces are applied. These forces can be associated to the change in resistivity measured at the output of the sensors.

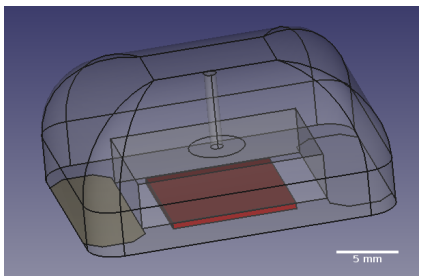

Figure 1: Design of the tactile sensor developed in this thesis. In red is represented the TMR sensor die and in grey the *EcoFlex* piece.

2. State of the art

2.1. Tactile sensing technologies

The main technologies for tactile sensing are based in capacitive, piezoresistive, piezoelectric, magnetic and optical methods. Capacitive tactile sensors are composed of 2 conductive plates (electrodes) with a layer of dielectric material between them. They detect the change in capacitance when a force is applied [3]. Piezoelectric sensors' active components are piezoelectric materials, these generate a voltage potential proportional to the deforming external forces which are measured by the sensors [4]. Piezoresistive tactile sensors work by detecting the change the electrical resistance of a material placed between or in touch with 2 electrodes [6] [15]. In Optical tactile sensors, when an external force is applied, the transmitting medium (optical fibers) is bent and such sensors can, for example, measure the change in light intensity at the output[12]. Magnetic tactile sensors measure changes in the magnetic field generated by a permanent magnet in their vicinity. When a force causes a displacement of the magnet and hence of the magnetic field, this will cause a voltage difference at the output of the sensor. Due to their high resolution and sensitivity, they were chosen to be used in these work. Among other types, they can be magnetoresistance based.

Magnetoresistance is the property of a material to change its resistance according to and applied external magnetic field. This change happens because of an existing dependence of the resistance of said material with the direction of the magnetization. It can be expressed by the following ratio:

$$MR(\%) = \frac{R_{min} - R_{max}}{R_{min}} \times 100 \qquad (1)$$

The values of R_{min} and R_{max} for a material can be obtained by sweeping the magnetic field applied to it while measuring the resistance. The sensors developed in this work apply the Tunnel Magnetoresistance (TMR) effect, in which the value of resistivity is changed on an insulating barrier when the relative orientation between the magnetization of layers of ferromagnetic material is changed by an external field.

2.2. Artificial skin

As referenced before, one can have a biomimetic approach to develop tactile sensing technologies, finding inspiration in nature for features of the sensors. In the case of artificial skin, the main source of inspiration is, of course, the human skin.

The human skin has several kinds of mechanoreceptors, capable of tactile sensing. Ruffini endings respond to pressure and stretch, while Merkel disks respond to pressure, texture and spatial deformations. Both of these mechanoreceptors are slow adaptors (SA), which means they send constant response to constant stimuli, hence are able to sense static forces [5]. On the other hand, Meissner's corpuscules respond well to as vibrations, while the Pacinian corpuscules are sensitive to high frequency stimuli and small deformations of skin. Both of these are rapid adaptors (RA) meaning that they have primarily dynamic response [14].

Artificial skin technologies for force/pressure sensing have been developed, mainly consisting of a transduction medium embedded in a rubber-like material, such as the corpuscles "embedded" in the skin sense forces. One of the recent developments in magnetic artificial skin is to use elastomers embedded with magnetic particles.

Such an artificial skin is presented by Yan et al [16]. In that work a prototype of sensor is presented using an artificial magnetic skin composed of a Hall sensor embedded in a layer of *EcoFlex* and a thin layer of sinusoidally magnetized PDMS film on top. The sensor was able to accurately measure normal and shear forces with a single unit and achieves super-resolved accuracy by deep-learning methods.

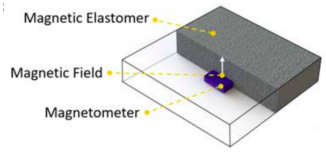

Figure 2: Magnetized artificial skin sensor presented in [7]

Another example of magnetic particle-embedded elastomeric artificial skin is reported by T. Hellebrekers et al [7] that consisted in an elastomer embedded with Ne-Fe-B particles. The change in the magnetic field is detected by a 3-axis magnetometer (Figure 2). Using machine learning based techniques the raw magnetic data is used to determine the intensity and location of the external force.

3. Theoretical Background

3.1. TMR effect and Magnetic tunnel junctions

3.1.1 The TMR effect

The TMR effect was first proposed by Julliere in 1975 [8] to explain the tunneling of electrons from one ferromagnetic layer to another through a sufficiently thin insulating barrier (the simplest form of a MTJ structure) when a voltage is applied between the 2 FM layers.

The current density for the parallel (J_P) and anti parallel (J_{AP}) configurations of the ferromagnetic layers of the MTJ are given by the expressions below, where $D_i(\uparrow \ / \ \downarrow)$, $i = 1, 2$ represent the density of spin up or down states for the ferromagnetic

layer i at the Fermi level (only these ones contribute to conduction).

$$\begin{aligned} J_P &\propto D_1(\uparrow)D_2(\uparrow) + D_1(\downarrow)D_2(\downarrow) \\ J_{AP} &\propto D_1(\uparrow)D_2(\downarrow) + D_1(\downarrow)D_2(\uparrow) \end{aligned} \tag{2}$$

The TMR effect in MTJs then originates from an existent difference between the density of spin up and spin down states in ferromagnetic materials at the Fermi level. This imbalance leads to the spin-dependent tunelling of electrons. This will lead to the dependence of the TMR(%) ratio on the relative direction of the magnetization of both ferromagnetic layers and their spin polarization, as depicted by Figure 3, in the following manner:

$$\begin{aligned} TMR(\%) &= \frac{R_{min} - R_{max}}{R_{min}} \times 100 \\ &= \frac{R_{AP} - R_P}{R_P} \times 100 = \frac{2P_1P_2}{1 - P_1P_2} \times 100 \end{aligned} \tag{3}$$

In this expression the polarization factors P_1 and P_2, of the ferromagnetic layers are given by

$$P = \frac{D(\uparrow) - D(\downarrow)}{D(\uparrow) + D(\downarrow)} \tag{4}$$

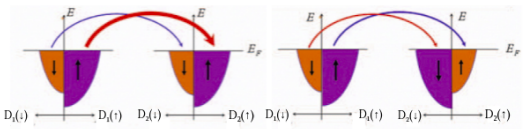

Figure 3: Schematic of density of states and spin dependent tunneling of electrons for the parallel configuration (left) and the anti parallel configuration (right) of the magnetization of ferromagnetic layers (adapted from [17]).

3.1.2 Magnetic Tunnel Junctions

As mentioned before, a MTJ in its most basic form is comprised of only a thin insulating barrier layer, usually AlO_x or MgO, sandwiched between two ferromagnetic layers. One of these layers is called the pinned layer, because of its fixed magnetization orientation, due to the exchange bias interaction with an adjacent anti-ferromagnetic (AFM) layer. The other layer is called the free one, because its magnetization orientation changes with the application of even small external magnetic fields.

The usual MTJ structure is also composed of buffer layers on top and bottom and a capping layer on top. The buffer provides protection and structural integrity and a low resistivity contact to the junction. The cap layer ends the stack of an MTJ and serves as protection against oxidation and etching for the layers below.

In the sensors used in this thesis, the pinned layer is replaced by a synthetic anti-ferromagnet (SAF) structure which consists of two ferromagnetic layers separated by a thin spacer layer. Due to the strong coupling between the 2 FM layers, the SAF structure increases the exchange field and it provides thermal stability to the MTJ.

Besides the SAF structure, a SFM (synthetic ferromagnetic) structure is also often used as a free layer. A soft magnet material such as NiFe is used adjacent to the CoFeB contributing to the low magnetic anisotropy of the free layer and reducing coercivity.

3.1.3 MTJ linearization strategies

Depending on the application, MTJs can be designed to have a hysteretic or a linear response (Figure 4), more appropriate for sensing applications. A linear response is achieved by making sure the relative direction of the magnetization of the free and pinned layers are orthogonal, in the absence of an external magnetic field.

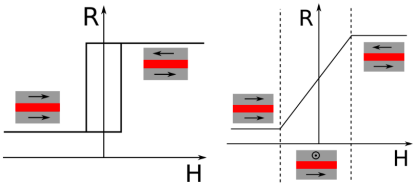

Figure 4: Transfer curves schematic for an MTJ: parallel anisotropies with hysteretic response (left) and orthogonal anisotropies with linear response (right). [10]

In this work, the linearization of the MTJs is achieved mainly by shape anisotropy by taking advantage of the self-demagnetizing field of the sensing layer which is created by controlling MTJ geometry, to set the anisotropy of the sensing layer perpendicular to the pinned layer. Since in a retangular shaped MTJ one has a free layer thickness much smaller than its width and height (W,h $\gg$ t), it is safe to assume that the layers magnetization is always in the sensor plane, as is its self-demagnetizing field. Under this assumption, we have from [9] the analytical solution for both components (width and height) of the self-demagnetizing field (H_d), as a function of the sensors' dimensions (w,h,t), and the saturation magnetization (M_s):

$$\begin{cases} H_d^h = -\frac{8M_s}{4\pi} \frac{t}{\sqrt{w^2+h^2}} \frac{w}{h} cos\theta \\ H_d^w = -\frac{8M_s}{4\pi} \frac{t}{\sqrt{w^2+h^2}} \frac{h}{w} sin\theta \end{cases} \tag{5}$$

Assuming the easy axis of the pinned layer is along the height of the MTJ, the sensor can then be designed to have a large aspect ratio and, as mentioned before, take advantage of shape anisotropy. With a higher aspect ratio w:h (of the order of 10:1), it is possible to set the anisotropy of the sensing layer perpendicular to that of the reference layer, because the H_d^w becomes more dominant [13].

This increase in aspect ratio also leads to an increased linear range but a decreased sensitivity in consequence.

3.2. Material Deformation

The strain (ϵ) vs stress (σ) relation of a material is usually used to describe the deformation it suffers. The stress can be seen as the force which the material is under, that causes the deformation, and the strain expresses this deformation when the stress is applied.

The behaviour in which the deformation is reversible is called elastic behaviour. In a strain vs stress plot the relation between the two variables is linear, and the slope is the Young modulus (E). As said before, the stress relates to the strain linearly by Hooke's law, as follows, where E is the Young modulus:

$$E = \frac{\epsilon}{\sigma} \tag{6}$$

However, hyperelastic materials can be put under very large stresses and recover their original shape which is why they are used in this work. The linear model presented before is not accurate when dealing with materials like these, hence a strain energy density function W is used to describe them, that relates the strain energy density of the material to the deformation.

The Generalized Rivlin Model where the strain energy density function is a polinomial that depends on the two invariants of the left Cauchy-Green deformation tensor I_1, I_2, is used to explain their behaviour. For incompressible materials, this function is as follows [11]:

$$W = \sum_{i,j=0}^{n} C_{ij}(I_1 - 3)^i (I_2 - 3)^j \tag{7}$$

where C_{ij} are material constants with $C_{00} = 0$ and $I_1 = \lambda_x^2 + \lambda_y^2 + \lambda_z^2$, $I_2 = \lambda_x^2\lambda_y^2 + \lambda_y^2\lambda_z^2 + \lambda_z^2\lambda_x^2$. Here λ_i are the principal stretch ratios at the point considered.

4. Microfabrication techniques/processes

The microfabrication of MTJ elements comprises various steps to obtain the final, working result. The sensors fabricated were deposited on a Si substrate. Each die composed of 16 sensors which in turn are made of 20 linearly aligned $20 \times 2\mu m^2$ MTJ elements.

The fabrication process starts with the MTJ pillars definition which begins with the deposition of the TMR stack and a *TiWn* cap layer on Si substrate, the stack deposited is schematically shown in Figure 5. This is followed by a lithography where the sample is coated with 1.5 μm of photoresist to protect the areas that correspond to the top of the MTJ elements' pillars. The photoresist will prevent the layers bellow it from being etched. The pillars are then defined by ion beam milling and the remaining resist is removed by ashing in the SPTS system.

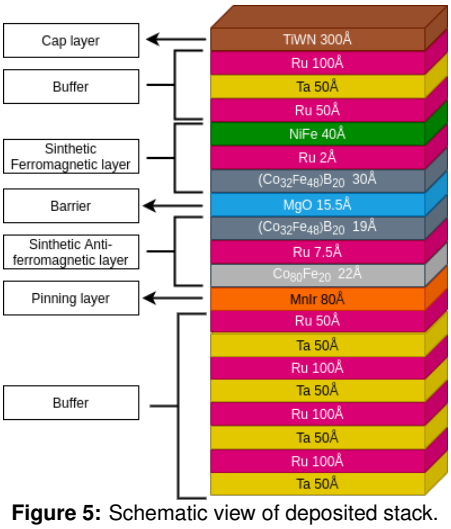

Figure 5: Schematic view of deposited stack.

The second part of the fabrication process is the definition of the bottom electrodes through the same processes as before, except this time resist is coated everywhere except the area where the bottom electrodes will be.

Lateral passivation to electrically insulate the top and bottom electrodes is the next step. It starts with the deposition of a 3000Å layer of SiO_2 by plasma-enhanced chemical vapour deposition (PECVD). A third lithography is then performed and the sample is then subject to reactive ion etching to open the vias and a resist ashing step is then performed to remove the remaining resist.

The passivation is followed by the definition of the top electrodes, which commences with a soft etch to remove impurities. A 3000Å layer of *AlSiCu* and a 150Å layer of *TiWn* are then deposited. This is again succeeded by a lithography to define the area of the top electrodes and finally a metal etch and a resist ashing step are performed in the SPTS system.

The final part of the process is opening the vias for the contact pads, which starts with the deposition a layer of SiO_2. A lithography to define the area of the vias is then performed, followed by reactive ion etch step and posterior resist ashing. The fabrication process is summarized in Figure 6.

After fabrication, the sample is diced to separate the sensor dies and the TMR sensors' transfer curve is then characterized. One of the dies is then mounted on a chip carrier and wirebonded. It is connected to a electronics acquisition board. Then it is time to fabricate the soft parts of the sensor which were made of the commercial silicon based elastomer *Ecoflex*^{TM} 00-30. Molds were

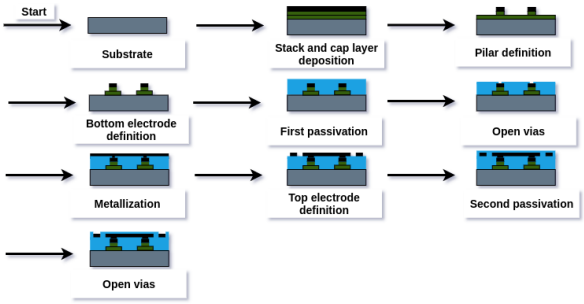

Figure 6: Summarized schematics of fabrication process of TMR sensors.

designed in the software *FreeCad* and 3D printed. 4 different pieces were produced with the goal of testing different magnetization distributions: with 1 permanent magnet, with 5 permanent magnets, with homogeneously distributed magnetic particles in a 40:60 (*EcoFlex*:Magnetic Particles) mass ratio, and with magnetic particle "islands", made of the same homogeneously magnetized elastomer. CAD drawings for the 4 elastomer configurations are shown in Figure 7

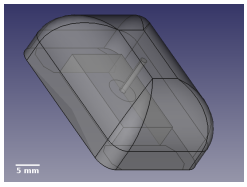

(a) *EcoFlex* piece with 1 permanent magnet, the magnet is inserted from the bottom of the piece until the top of the cylinder hole.

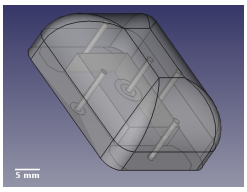

(b) *EcoFlex* piece with 5 permanent magnets, the magnets are inserted from the bottom of the piece until the top of the 5 cylinders holes.

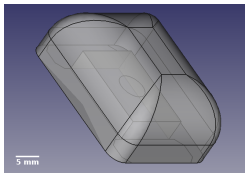

(c) *EcoFlex* piece homogeneously magnetized with magnetic particles.

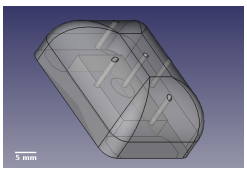

(d) *EcoFlex* piece with 5 magnetic particle "islands", the mixture of *EcoFlex* and Magnetic Particles at a 40:60 mass ratio is injected into the cylinder holes.

Figure 7: CAD drawings for the 4 *EcoFlex* pieces used in this work.

The magnets these were embedded in the elastomer piece in such a way as to align the direction of their magnetic moment with the sensitive direction of the TMR sensors. The pieces with magnetized *EcoFlex* were annealed for 1 hour and a half at 135ºC in the presence of a 1T magnetic field in such a way as to also align their magnetic moment with the TMR sensors' sensitive direction.

5. Simulations

A simulated model of the deformation of the elastomers used in this work is developed and the simulated data are validated against experimental data obtained in the real elastomer. The simulation was made using a finite element method (FEM) with the *COMSOL Multiphysics 5.5* software. Since in the literature there weren't any satisfying reports of the mechanical properties of the elastomer used in these work, an experimental uniaxial traction test was also performed in both pure and magnetized *EcoFlex*. The data obtained from this test was then fitted to obtain linear and hyperelastic model parameters that are used in the simulations.

5.1. Uniaxial traction tests

Since the mechanical properties and consequently the hyperelastic model parameters change significantly depending on the preparation and conditions of cure, in order to obtain the Young's Modulus and the hyperelastic model parameters needed for the simulations, an uniaxial traction test was performed on both materials. The resulting stress vs strain data was fitted to several models in order to obtain the parameters needed, as shown Figures 8 and 9, where R^2_{MR} refers to the values of the R^2 parameter when fitting data with the 2 parameter Mooney-Rivlin mode, and R^2_{NH} when fitting with the Neo-Hookean model. The fits are made assuming isotropy and incompressibility of the material and the results are fitted to the the first Piola-Kirchhoff stress expressions for uniaxial deformation [1]:

- Neo-Hookean model: $P_1 = \mu(\lambda - \lambda^{-2})$
- Mooney-Rivlin of 2 parameters: $P_1 = 2(1 - \lambda^{-3})(\lambda C_{10} + C_{01})$
- Mooney-Rivlin of 5 parameters: $P_1 = 2(1 - \lambda^{-3})(\lambda C_{10} + 2C_{20}\lambda(\lambda^2 + \frac{2}{\lambda} - 3) + C_{11}\lambda(2\lambda + \frac{1}{\lambda^2} - 3) + C_{01} + 2C_{02}(2\lambda + \frac{1}{\lambda^2} - 3) + C_{11}(\lambda^2 + \frac{2}{\lambda} - 3))$

where λ is the strain and μ, C_{10}, C_{01}, C_{20}, C_{02} and C_{11} are the parameters to obtain.

It is noticeable that the expressions fit the results quite well, with values of R^2 bigger than 97% for each of the fitted models for magnetized elastomer and bigger than 86% for pure *EcoFlex*. The 2 parameter Mooney-Rivlin model and the Neo-Hookean model aren't adequate to model the behaviour of materials under large deformations: this explains the poor fit obtained when trying to fit the experimental data with these models in the whole domain. With this under consideration, they were used to fit only small strains, in the order of 2/3 times.

From this fits to the experimental data, the hyperelastic models' parameters were obtained,

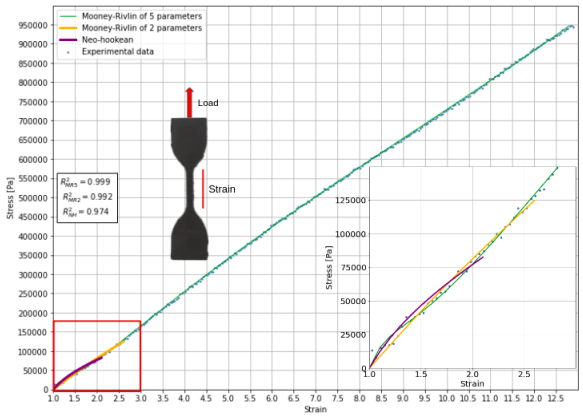

Figure 8: Experimental uniaxial traction test results and fitted models for one tensile specimen of magnetized *EcoFlex*.

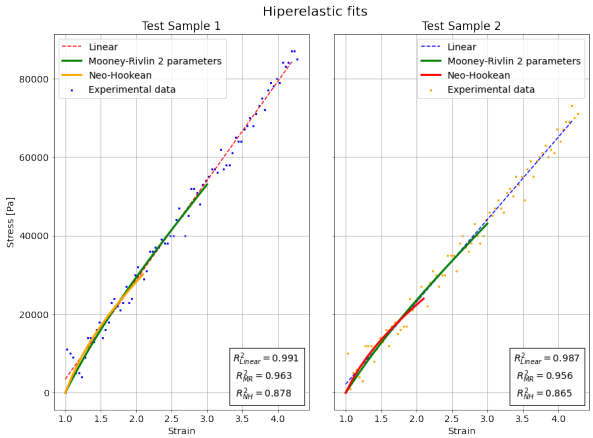

Figure 9: Experimental uniaxial traction test results and fitted models for both tensile specimen of pure *EcoFlex*.

to be used in the simulation model developed. These parameters are the following, for magnetized *EcoFlex*:

- Neo-Hookean: $\mu = 42315.49\ N/m^2$
- 2 parameter Mooney-Rivlin: $C_{10} = 32017.66$ Pa; $C_{01} = -20336.20$ Pa;
- 5 parameter Mooney-Rivlin: $C_{10} = -60575.00$ Pa; $C_{01} = 92823.04$ Pa; $C_{20} = -12.12$ Pa; $C_{02} = 28818.60$ Pa; $C_{11} = -450.97$ Pa;

and for pure *EcoFlex*:

- Linear: $E = 23113.09$ Pa
- Neo-Hookean: $\mu = 14445.55\ N/m^2$;
- 2 parameter Mooney-Rivlin: $C_{10} = 9831.74$ Pa; $C_{01} = -4556.83$ Pa;

5.2. Deformation Simulations

The goal of this simulation is to study the behaviour of the elastomer as a function of an applied force. This is achieved through the data of applied force on the indenter in relation to its displacement as it pushes on the elastomer. To obtain the data experimentally, a force sensor is placed orthogonally to the top-most face of the *EcoFlex* part and lowered by increments of $\approx 55\mu m$ until it reaches $\approx 4400\mu m$, exerting a normal force on the *Ecoflex*. The simulation was modelled after this experiment. The geometry of the *EcoFlex* piece was imported from a CAD drawing which was also used in the fabrication of the elastomer pieces used for experimental tests and the indenter is modeled after the force sensor which was used to apply the force experimentally (Figure 10).

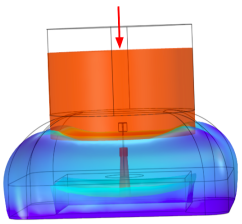

Figure 10: Deformation of *EcoFlex* piece with 1 permanent magnet (blue) by indenter (red).

Several material deformation models are tested in the simulations of the deformation of the pieces. A Linear elastic model, for which the following relation applies:

$$\epsilon = \frac{1}{2}(\nabla u + \nabla u^T) \tag{8}$$

where ϵ is the strain tensor and u is the displacement vector.

The Generalized Rivlin Model, of which the 2, 5 and Neo-Hookean (when $C_{ij\neq 10} = 0$) models were used:

$$W = \sum_{i,j=0}^{n} C_{ij}(I_1 - 3)^i (I_2 - 3)^j \tag{9}$$

The results obtained are presented in Figures 12 and 11.

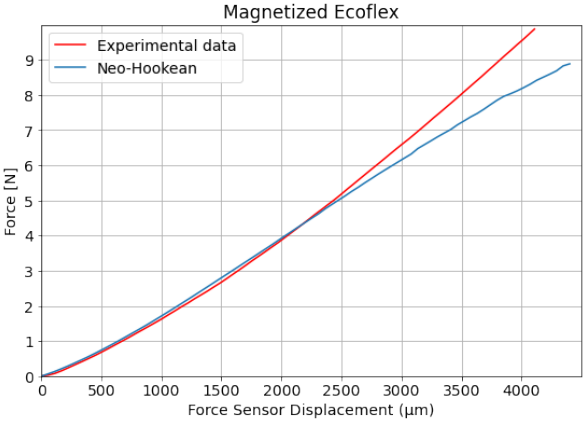

Figure 11: Simulation results and comparison to experimental data for magnetized elastomer.

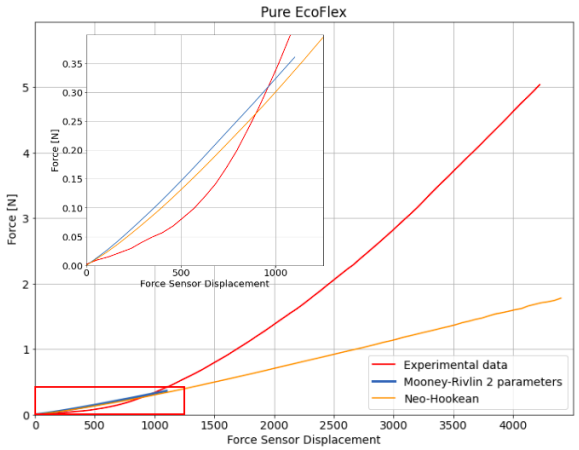

Figure 12: Simulation results and comparison to experimental data for pure elastomer.

For the magnetized *EcoFlex* pieces, the Neo-Hookean model presents a maximum error of the order of 15% in relation to the experimental data for bigger deformations, which constitutes a good result for FEM simulations.

As for the pure *EcoFlex* pieces, one can see that even for the the smaller deformations, the error is still too big for any of the models used (around 35% for the Neo-Hookean model). It is also evident that none of the two models considered behaves similarly to the experimental case, which means that a good FEM simulation was not achieved in this case.

6. Results

6.1. Force test Setup

A motorized precision movement stage is used in combination with the ATI Force and torque *Nano17* sensor to test the magnetic sensors designed. The force test setup was composed of the magnetic sensor and the magnetized *EcoFlex* piece, the data acquisition board and the force sensor, which was attached to the Z axis of the stage and made to apply a force on the *EcoFlex* by its movement. An image of the setup is shown below (Figure 13).

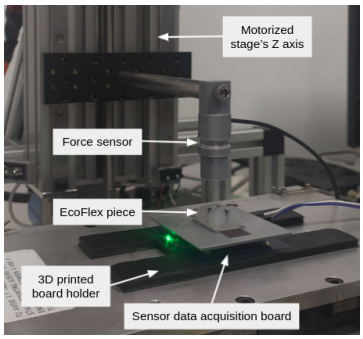

Figure 13: Setup for experimental data acquisition.

Using this setup, for each of the *EcoFlex* pieces several experiments were performed: one for the stability test, one for the simulation detailed in the previous section and one for the estimation of force intensity and location. These experiments are all detailed in the respective results sections.

6.2. TMR sensors characterization

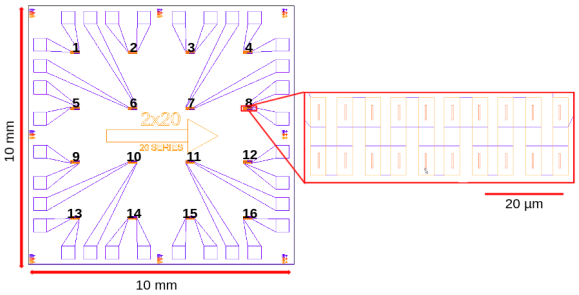

Figure 14: CAD mask used for the fabrication of the TMR sensors with numbered sensors (left) and CAD mask detail of a single sensor comprised of 20 MTJs connected in series (right)

In Figure 14, the CAD mask used in the fabrication of the TMR sensors is represented.

The magnetotransport curves were taken for each sensor. An example of such a curve for one of the TMR sensors is presented in Figure 15.

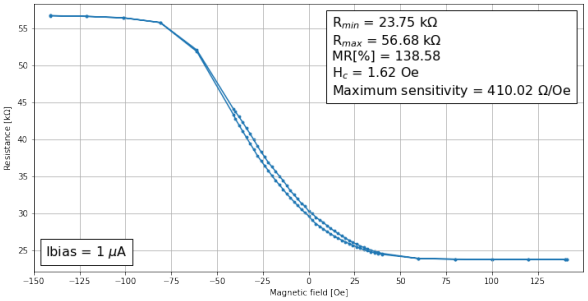

Figure 15: Example magnetotransport curve for sensor 1 with relevant parameters.

The other sensors response are similar, the maximum sensitivity varies in the range of [385.30 Ω/Oe, 561.25 Ω/Oe] which is a good sensitivity value for the application at hand. As for the MR[%] it varies in the range of [116.68,142.85] which are normal values for MgO barrier MTJs.

6.3. Sensor Stability test

The stability test consisted in using the force sensor as an indenter and move it down until it was approximately 3500 μ into the *EcoFlex* piece for 3 seconds and then move it up until the force applied on the elastomer piece was zero for another 3 seconds. The results of this test are shown in Figure 16, .

In this plot, each iteration represents a step of lowering or lifting the force sensor into or from the elastomer piece. The points represent the average taken of the output of the sensor during the 3 seconds of each step. Due to the similarity between

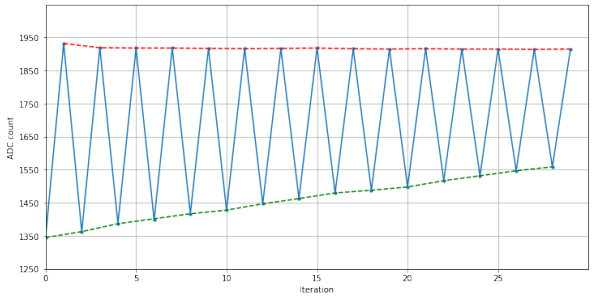

Figure 16: Plot of output of one of the TMR sensors in ADC counts in each iteration.

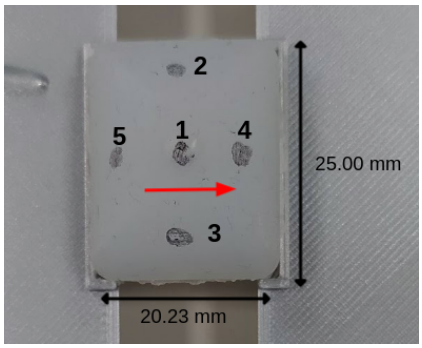

Figure 17: *EcoFlex* piece with the different application points marked on its surface. The red arrow represents the sensitive direction of the sensors.

the behaviour of all the TMR sensors in these experiment, the stability plot of only one TMR sensor is presented.

As one can observe, the response of the sensor when the elastomer piece is not being actuated on, represented in the plot by the red dashed line, is very constant from which can be concluded that there isn't a biasing in the sensors, that is, for the same force applied on the elastomer (0N in this case), the sensors output the same result. This means that the change of the magnetic field is completely reverted after a deformation of the piece, thus it can be inferred that the *EcoFlex* piece comes back to its initial form even after large deformations.

As for the points corresponding to when there is a force applied on the elastomer, we notice a clear upwards trend which is explained by the precision stage moving a distance which is a little bit different than the one ordered in each iteration, which causes it to move into the elastomer piece a little less each time, thus applying a smaller force. So, this has nothing to do with the stability of the sensor or lack there of.

6.4. Force intensity and location sensing

The data was acquired by the following procedure: in 5 different application points, a normal force was applied by a 3D printed indenter fitted in the force sensor that allows for the force to be applied in a much smaller application point. The normal force was applied by moving the force sensor until it was directly above the application point and at the same height as the surface of the elastomer piece in that point. 80 steps were then made where the force sensor was moved $50\mu m$ down into the piece and the output of the 16 sensors saved in a file, as well as the output of the force sensor and a number that serves as an identifier of the application point (Figure 17, in the figure is also represented the sensitive direction of the sensors by the red arrow).

To analyze the data obtained from this a simple machine learning model was trained. For the estimation of the intensity of the force, a Random Forest regression was used. The number of decision trees used in the Random forest regression was 100. Since not many data points were acquired in the experiments, the leave one out cross-validation strategy was used to estimate the performance of the model. This method of cross-validation is very computationally expensive, which is why it is not used unless in small datasets. This model was trained and fitted into the data gathered for the 5 application points for all the different types of *EcoFlex* pieces. The inputs of the model are the ADC counts obtained from each of the 16 TMR sensors.

The model generally estimates the force quite well, especially for the *EcoFlex* pieces with 5 permanent magnets and with distributed magnetization. As for the other elastomer pieces, the model doesn't work quite as well, with a high number of outliers and a higher error than in other cases (Table 1.)

It is worthy of mention that there appears to be a bias in the force estimates, since there appears to be a pattern in the outliers over the 4 elastomer configurations (Figure 18).

	1 PM	5 PM	Distributed MPs	MP islands
R^2	0.835	0.993	0.988	0.940
MAE [N]	0.101	0.027	0.069	0.083

Table 1: R^2 and mean absolute error for the regression model, for each configuration of the *EcoFlex* pieces.

The higher values of MAE and lower R^2 for the one permanent magnet case, might be explained by the fact that the magnetic field comes only from one point in the elastomer piece, which makes it difficult to estimate the intensity of the force through just the output of the sensors.

In the case of the elastomer piece with the magnetic particle "islands", an explanation for the bigger MAE might be that the they are symmetrical in pairs in relation to the x and y axes, which might cause the changes of the magnetic field to cancel when a force is applied since two of them will deform in opposite directions.

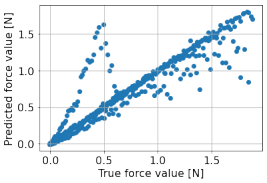

(a) *EcoFlex* piece with 1 permanent magnet.

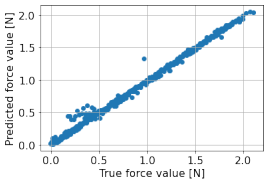

(b) *EcoFlex* piece with 5 permanent magnets.

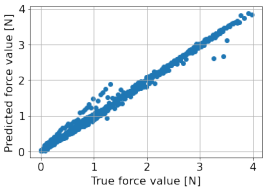

(c) *EcoFlex* piece magnetized with magnetic particles.

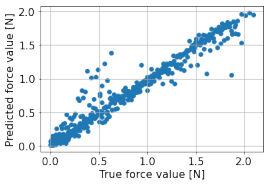

(d) *EcoFlex* piece with 5 magnetic particle "islands".

Figure 18: Estimated versus true force plots for each *EcoFlex* piece.

To estimate the position of the force, the strategy was to attribute a class to each application point use a classifier to distinguish between the different application points (Figure 17).

A support vector machine (SVM) classifier was used in this step. This is a supervised learning algorithm that takes data points and outputs the hyperplane that best separates the classes. The model was trained and fit to the data and the leave one out cross-validation strategy was also used. The inputs of the model are the ADC counts obtained from each of the 16 TMR sensors.

	1 PM	5 PM	Distributed MPs	MP islands
Accuracy	0.98	1.00	0.98	0.97

Table 2: Accuracy of classifier for each elastomer piece.

As can be observed in Table 3, the SVM classifier is very accurate in estimating the class of the data, with almost 100% accuracy in every elastomer piece.

Finally, because the estimation of the force had an high MAE for the elastomer piece with one permanent magnet and for the piece with magnetic particle "islands", the same random forest regression model was used to estimate the force, but this time assuming the class was already known (by giving the class as an input to the model as well), results are shown in Figure 19.

By comparing the two plots with the first ones obtained without considering the class an input, the improvement is evident. The MAE for both the situations lowers as there are also less outliers and the R^2 value improves, as can be seen in Table 3. This results are an indication that if the position of the force is estimated in the first place, the model will more accurately estimate the force afterwards.

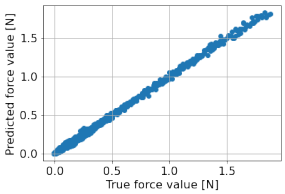

(a) *EcoFlex* piece with one permanent magnet.

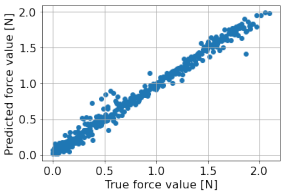

(b) *EcoFlex* piece with 5 magnetic particle "islands".

Figure 19: Estimated versus true force plots for each *EcoFlex* piece considered.

	1 PM	MP islands
R^2	0.998	0.982
MAE [N]	0.020	0.053

Table 3: R^2 and mean absolute error for the regression model for both situations considered.

7. Conclusions

The work developed in this thesis had the goal of developing a tactile sensor capable of detecting forces and their locations through a simple setup. The sensor was designed as a magnetized artificial flexible skin using *EcoFlex*, with a 4×4 matrix of TMR sensors, all with the same sensing direction, used to detect the changes in magnetic field when a force deformed the magnetized elastomer piece.

A FEM simulation was used to simulate the behaviour of the sensor, namely the voltage vs magnetic field characteristic of the sensor, by mimicking the physical parameters of the system at hand. An uniaxial tensile test was performed on both homogeneously magnetized *EcoFlex* (60:40 mass ratio of *EcoFlex*:MPs) and pure *EcoFlex* specimens to obtain their strain vs stress curve and fit to several material models. The deformation simulation was successful in describing the deformation of homogeneously magnetized *EcoFlex*, which was validated against experimental force data acquired, with a maximum error of approximately 15% for the whole deformation domain. However, it failed to do so for pure *EcoFlex*, as previously mentioned this might be due to various factors such as the fact that performing only uniaxial traction testing gave an incomplete description of the mechanical properties of the material, or the fact that the *EcoFlex* used in these specimen was an old batch which was noted to have different mechanical properties than newer batches.

The fabricated sensors were tested to determine their electrical stability and the ability to differentiate force intensity and localization. Four different sensors were tested, being the difference in the *EcoFlex* pieces used as the source of the stray field for the TMR sensors to detect.

The *EcoFlex* proved very stable when being actuated repeatedly during 30 iterations between a

fixed deformation and no deformation, giving a constant ADC counts output for the same force applied.

By using a random forest regression model, all the sensor configurations were able to estimate the intensity of normal forces with a good fit to the model and a low mean absolute error of approximately 0.1N for the *EcoFlex* with one permanent magnet, 0.02N for the one with 5 permanent magnets, 0.07 for the homogeneously magnetized *EcoFlex* configuration, and 0.08 for the configuration with magnetic particle "islands". Although the first and last mentioned had a value of R^2 slightly lower than the other two.

It was also demonstrated the ability of the sensors to differentiate between 5 different points of application of the forces, by using a support vector machine classifier, with a minimum accuracy over configurations of 0.97.

Future work would include, in short term, the development of a simulated model for the magnetic field in the TMR sensors' positions when the elastomer is actuated. The acquisition of more force data over all the area of the *EcoFlex* pieces with the goal of generalizing the estimation of the location of the forces applied. Also compression tests should be made on *EcoFlex* test specimen to obtain better parameters for the simulations.

References

[1] Fitting measured data to different hyperelastic material models. https://br.comsol.com/blogs/fitting-measured-data-to-different-hyperelastic-material-models/. Accessed: 2021-10-22.

[2] B. D. Argall and A. G. Billard. A survey of tactile human–robot interactions. *Robotics and Autonomous Systems*, 58(10):1159–1176, 2010.

[3] C. Chi, X. Sun, N. Xue, T. Li, and C. Liu. Recent progress in technologies for tactile sensors. *Sensors*, 18(4), 2018.

[4] R. S. Dahiya, L. Lorenzelli, G. Metta, and M. Valle. Posfet devices based tactile sensing arrays. In *Proceedings of 2010 IEEE International Symposium on Circuits and Systems*, pages 893–896, 2010.

[5] J. Dargahi and S. Najarian. Human tactile perception as a standard for artificial tactile sensing—a review. *The international journal of medical robotics + computer assisted surgery : MRCAS*, 1:23–35, 11 2004.

[6] P. S. Girão, P. M. P. Ramos, O. Postolache, and J. Miguel Dias Pereira. Tactile sensors for robotic applications. *Measurement*, 46(3):1257–1271, 2013.

[7] T. Hellebrekers, O. Kroemer, and C. Majidi. Soft magnetic skin for continuous deformation sensing. *Advanced Intelligent Systems*, 1(4):1900025, 2019.

[8] M. Julliere. Tunneling between ferromagnetic films. *Physics Letters A*, 54(3):225–226, 1975.

[9] S. Liao, S. Yuan, and H. Bertram. Biasing characteristics of unshielded, boundary exchange-coupled sal/mr sensors. *IEEE Transactions on Magnetics*, 29(6):3873–3875, 1993.

[10] P. Ribeiro. Ciliary structure inspired force sensor for robotic platforms. Master's thesis, Insituto Superior Técnico, 2016.

[11] R. S. Rivlin and D. W. Saunders. Large Elastic Deformations of Isotropic Materials. VII. Experiments on the Deformation of Rubber. *Philosophical Transactions of the Royal Society of London Series A*, 243(865):251–288, Apr. 1951.

[12] D. Sartiano and S. Sales. Low cost plastic optical fiber pressure sensor embedded in mattress for vital signal monitoring. *Sensors*, 17(12), 2017.

[13] A. V. Silva, D. C. Leitao, J. Valadeiro, J. Amaral, P. P. Freitas, and S. Cardoso. Linearization strategies for high sensitivity magnetoresistive sensors. *European Physical Journal-applied Physics*, 72:10601, 2015.

[14] D. Silvera-Tawil, D. Rye, and M. Velonaki. Artificial skin and tactile sensing for socially interactive robots: A review. *Robotics and Autonomous Systems*, 63:230–243, 2015. Advances in Tactile Sensing and Touch-based Human Robot Interaction.

[15] K. Weiss and H. Worn. The working principle of resistive tactile sensor cells. *IEEE International Conference Mechatronics and Automation, 2005*, 1:471–476 Vol. 1, 2005.

[16] Y. Yan, Z. Hu, Z. Yang, W. Yuan, C. Song, J. Pan, and Y. Shen. Soft magnetic skin for super-resolution tactile sensing with force self-decoupling. *Science Robotics*, 6(51):eabc8801, 2021.

[17] J.-G. J. Zhu and C. Park. Magnetic tunnel junctions. *Materials Today*, 9(11):36–45, 2006.